Distinct Cell Adhesion Signature Defines Glioblastoma Myeloid-Derived Suppressor Cell Subsets

Defne Bayik[1,2], Cynthia F. Bartels[3], Katreya Lovrenert[3], Dionysios C. Watson[1,2,4], Duo Zhang[5], Kristen Kay[1], Juyeun Lee[1], Adam Lauko[1,6,7], Sadie Johnson[1], Alice Lo[1], Daniel J. Silver[1,2], Mary McGraw[8], Matthew Grabowski[8], Alireza M. Mohammadi[8], Filippo Veglia[9], Yi Fan[5], Michael A. Vogelbaum[10], Peter Scacheri[2,3], and Justin D. Lathia[1,2,8]

ABSTRACT

In multiple types of cancer, an increased frequency in myeloid-derived suppressor cells (MDSC) is associated with worse outcomes and poor therapeutic response. In the glioblastoma (GBM) microenvironment, monocytic (m) MDSCs represent the predominant subset. However, the molecular basis of mMDSC enrichment in the tumor microenvironment compared with granulocytic (g) MDSCs has yet to be determined. Here we performed the first broad epigenetic profiling of MDSC subsets to define underlying cell-intrinsic differences in behavior and found that enhanced gene accessibility of cell adhesion programs in mMDSCs is linked to their tumor-accelerating ability in GBM models upon adoptive transfer. Mouse and human mMDSCs expressed higher levels of integrin β1 and dipeptidyl peptidase-4 (DPP-4) compared with gMDSCs as part of an enhanced cell adhesion signature. Integrin β1 blockade abrogated the tumor-promoting phenotype of mMDSCs and altered the immune profile in the tumor microenvironment, whereas treatment with a DPP-4 inhibitor extended survival in preclinical GBM models. Targeting DPP-4 in mMDSCs reduced pERK signaling and their migration towards tumor cells. These findings uncover a fundamental difference in the molecular basis of MDSC subsets and suggest that integrin β1 and DPP-4 represent putative immunotherapy targets to attenuate myeloid cell-driven immune suppression in GBM.

Significance: Epigenetic profiling uncovers cell adhesion programming as a regulator of the tumor-promoting functions of monocytic myeloid-derived suppressor cells in glioblastoma, identifying therapeutic targets that modulate the immune response and suppress tumor growth.

Introduction

Glioblastoma (GBM), the most common primary malignant brain tumor, is characterized by a dramatic infiltration of immunosuppressive myeloid cells, which can comprise 30% to 50% of the tumor mass (1). Accumulation of these myeloid cells represents a critical barrier to treatment of GBM, and their targeting improves response to radiotherapy and immunotherapy in preclinical models (2–4). Myeloid-derived suppressor cells (MDSC), a heterogeneous population of immature cells that originate in the bone marrow, constitute one of the immunosuppressive myeloid cell populations in GBM together with tumor-associated macrophages and microglia, albeit they are observed at a lower frequency (1). Biomarker studies further established that MDSCs expand in the peripheral circulation of patients with GBM compared with those with low-grade brain malignancies, accumulate in tumors and associate with worse disease outcome (5–7). These observations have served as the basis for the development and assessment of anti-MDSC therapies in GBM and other advanced cancers (8–10).

MDSCs are classified into two phenotypically and functionally distinct subsets, monocytic (mMDSC) and granulocytic/polymorphonuclear (gMDSC; ref. 1). Although both subsets can interfere with the activity of cytotoxic T cells, recent studies demonstrate that they undertake additional roles both systemically and within the tumor microenvironment. In breast cancer models, it was demonstrated that mMDSC localization to primary tumors drives a stem cell phenotype, whereas gMDSCs facilitate metastatic spread to the lungs (11). Assessment of MDSC subsets also revealed a difference in their localization in GBM. mMDSCs represented the dominant subtype in both mouse and human tumors and were especially enriched in male tumors (4, 12). This was in part driven by differential response to chemoattractants by MDSC subtypes. Both the CCL2-CCR2 and the macrophage migration inhibitory factor (MIF)-CD74 axes have been implicated in the recruitment of mMDSCs to the GBM microenvironment (13, 14). However, the molecular basis of distinct MDSC subset trafficking and function in the context of solid malignancies, including GBM, remains unclear. We hypothesized that differences in epigenetic programming can inform distinct behavior of MDSC subsets and performed Assay for Transposase-Accessible Chromatin with high-throughput sequencing (ATAC-seq) to identify unique pathways linked to MDSC subset function, trafficking or interaction with the

[1]Lerner Research Institute, Cleveland Clinic, Ohio. [2]Case Comprehensive Cancer Center, Cleveland, Ohio. [3]Department of Genetics and Genome Sciences, Case Western Reserve University, Cleveland, Ohio. [4]University Hospitals Cleveland Medical Center, Cleveland, Ohio. [5]Department of Radiation Oncology, University of Pennsylvania, Philadelphia, Pennsylvania. [6]Department of Pathology, Case Western Reserve University, Cleveland, Ohio. [7]Case Western Reserve University, Medical Science Training Program, Cleveland, Ohio. [8]Rose Ella Burkhardt Brain Tumor Center, Cleveland Clinic, Ohio. [9]Department of Immunology, Moffitt Cancer Center, Tampa, Florida. [10]Department of Neuro-oncology, Moffitt Cancer Center, Tampa, Florida.

Corresponding Authors: Justin D. Lathia, Department of Cardiovascular and Metabolic Sciences, Cleveland Clinic Lerner Research Institute, 9500 Euclid Avenue, NC-10, Cleveland, OH 44195. E-mail: lathiaj@ccf.org; and Defne Bayik, Department of Cardiovascular and Metabolic Sciences, Cleveland Clinic Lerner Research Institute, 9500 Euclid Avenue, NE3-214, Cleveland, OH 44195. E-mail: watsond3@ccf.org

tumor microenvironment. Our results highlight that cell adhesion programming genes are more accessible in mMDSCs and demonstrate that integrin β1 and dipeptidyl peptidase-4 (DPP-4) contribute to the distinct protumorigenic function of mMDSCs.

Materials and Methods

Cell lines

GL261 cells were obtained from the Developmental Therapeutics Program, NCI, and the SB28 line was gifted by Dr. Hideho Okada (University of California). Cells were maintained in RPMI1640 (Media Preparation Core, Cleveland Clinic) supplemented with 10% FBS (Thermo Fisher Scientific) and 1% penicillin/streptomycin (1% Pen/Strep, Media Preparation Core). All cell lines were treated with 1:100 MycoRemoval Agent (MP Biomedicals) upon thawing and routinely tested for *Mycoplasma* spp. (Lonza). Cells were not used beyond passage number 20.

Antibodies

For sorting and immune profiling, the following antibodies were purchased from BioLegend, unless otherwise specified: Gr-1 (clone RB6–8C5, 11–5931–85, eBioscience or clone RB6–8C5, 108407), CD11b (clone M1/70, 563553; BD Biosciences), CD11c (clone HL3, 612796; BD Biosciences), Ly6G (clone 1A8, 560603; BD Biosciences), CD3 (clone 145–2C11, 56379; BD Biosciences), γδ TCR (clone GL3, 562892; BD Biosciences), CD69 (clone, H1.2F3, 741234; BD Biosciences), CD29 (clone Huts-4, MAB2079Z; Millipore Sigma), I-A/I-E (clone M5/114.15.2, 107606), CD68 (clone FA-11, 137024), Ly6C (HK1.4, 128024, 128032 or 128044), Ly6G (clone 1A8, 127618, 127648 or 127639), CD11b (M1/70, 101212), NK1.1 (clone PK136, 108716 or 108730), B220 (clone RA3–6B2, 103237), CD45 (clone 30F-11, 103138), CD45.2 (clone 104, 109808), CD8 (clone 341, 748879 or clone 53–6.7, 553034; BD Biosciences), CD29 (clone 30F-11, 103132), CD18 (clone M18/2, 101407), integrin β7 (clone FIB504, 321225), CD8 (clone 53–6.7, 100712), CD4 (clone GK1.5, 100422 or clone RM4–5, 560468; BD Biosciences), PD-1 (clone 29F.1A12, 135241), F4/80 (clone BM8, 123118), CD40 (clone 3/23 124610), PD-L1 (clone 10F.9G2, 124321), and CD206 (clone C068C2, 141731).

InVivoMAb anti-mouse CD29 (clone KMI6, BE0232), InVivoMAb anti-mouse/human integrin β7 (clone FIB504, BE0062), and InVivo-MAb rat IgG2a isotype control, anti-trinitrophenol (clone 2A3, BE0089) antibodies were purchased from BioXCell.

For assessment of patient specimens, fluorophore-conjugated CD45 (clone HI30, 560777), CD33 (clone WM53, 562492), CD14 (clone M5E2, 558121), CD11c (clone 3.9, 748288), CD3 (clone SP34–2, 557757), and ITGB7 (clone FIB504, 555945) were purchased from BD Biosciences. CD19 (clone HIB19, 302218), CD56 (clone HCD56, 318332), Lox1 (clone 15C4, 358606), CD11b (clone ICRF44, 301332), CD66b (clone G10F5, 305114), HLA-DR (clone L243, 307638), CD29 (clone TS2/16, 303016), CD18 (clone CBR LFA-1/2, 366310), ITGB7 (clone FIB504, 121006), and CD68 (clone Y1/82A, 333814) were acquired from BioLegend.

Mice

All animal experiments were approved by the Cleveland Clinic Institutional Animal Care and Use Committee (IACUC) and performed in accordance with the guidelines. Four-week-old C57BL/6 male and female mice (JAX Stock #000664) were purchased from the Jackson Laboratory as required and housed in the Cleveland Clinic Biological Research Unit Facility. Four-week-old NOD.Cg-Prkdc SCID Il2rg tm1Wjl /SzJ male mice were bred in-house. Mice were

intracranially injected at 4 to 8 weeks old with 25,000 to 30,000 GL261 or 10,000 to 30,000 SB28 cells in 5 µL RPMI null media into the left cerebral hemisphere 2 mm caudal to the coronal suture, 3 mm lateral to the sagittal suture at a 90° angle with the murine skull to a depth of 2.5 mm, using a stereotaxis apparatus (Kopf). Mice were monitored daily for neurologic symptoms, lethargy and hunched posture that would qualify as signs of tumor burden. For all experiments, mice were randomized at the time of treatment or adoptive transfer, and co-housed to limit cage effect. To analyze the effects of drugs, mice implanted with GL261 and SB28 were intraperitoneally injected with 25 mg/kg sitagliptin (Cayman Chemical) or PBS for 2 weeks. The first dose was administered right after the tumor implantations, and a 5 days on 2 days off cycle was followed.

Adoptive transfer

For adoptive transfer, recipient mice were implanted with tumors as described above. A separate cohort of mice were implanted with tumors to obtain donor MDSCs for transfer. Femur and tibia from donor mice were flushed with 10 mL PBS and strained through 40 µm filter (Thermo Fisher Scientific). Cells were centrifuged at $400 \times g$ for 5 minutes and incubated with 1:25 diluted mouse FcR blocking reagent (Miltenyi Biotec, 130–092–575) in FACS buffer (PBS, 5 mmol/L EDTA and 2% FBS) on ice for 10 minutes. Samples were stained with a combination of 1:100 diluted CD11b, Gr-1, and Ly6G in the presence of FcR blocking reagent for 15 minutes on ice. Cells were resuspended at a concentration of 1 to 2 million/mL. mMDSCs (CD11b$^+$Gr-1$^+$Ly6G$^−$) and gMDSCs (CD11b$^+$Gr-1$^+$Ly6G$^+$) were sorted into FACS buffer using a BD FACSMelody (BD Biosciences) using a nozzle size of 100 µmol/L, sheath pressure of 20 psi, and event rate of 3,000 to 5,000 events/seconds. The sort efficiency was confirmed to be between 75% and 85%, and the cell viability was >75%. After centrifugation at $400 \times g$ for 5 minutes, the cells were resuspended in PBS at a concentration of 400,000 per 50 µL. In some experiments, sorted MDSCs were treated *ex vivo* with 100 µg/mL isotype control, anti-integrin β1 or anti-integrin β7 antibodies (BioXcell) for 1 hour on ice prior to transfer. Mice were anesthetized with isoflurane, and cells were retro-orbitally transferred using 27G needles (Exel).

Immune profiling

GL261-bearing mice were adoptively transferred with MDSC subsets as described above, and mice were euthanized 3 days later. For immune profiling in the SB28 model, mice were implanted with 15,000 tumor cells, adoptively transferred with MDSCs 4 days later and euthanized after 3 days. GL261-bearing mice that were treated with sitagliptin were euthanized when the first animal was at endpoint (day 18 for repeat 1 and day 16 for repeat 2). Cardiac blood was collected into EDTA-coated Safe-T-Fill micro capillary blood collection tubes (RAM Scientific). Samples were centrifuged at $1,000 \times g$ for 10 minutes at 4°C to separate the serum, and cells were used for subsequent staining. Bone marrow was flushed from one femur and tibia in 5 mL PBS and passed through a 40 µm strainer to obtain single cells. Tumors were resected from the left hemisphere. From sham-injected controls, an equal volume of healthy brain tissue was removed. Tissue were mashed on a 40 µm strainer and washed with PBS before transferring into 96-well round-bottom plates (Thermo Fisher Scientific). Samples were stained with 1:1,000 diluted LIVE/DEAD Fixable Stains (Thermo Fisher Scientific, L34962) in PBS for 10 minutes on ice. Following a wash step, cells were resuspended in FcR Blocking Reagent (Miltenyi Biotec) at a 1:25 dilution in PBS/2% BSA (Sigma-Aldrich) for 10 minutes on ice. Fluorophore-conjugated antibodies diluted 1:50 were added to suspensions, and cells were further incubated for

20 minutes on ice. Samples were washed with PBS/BSA and fixed overnight in eBioscience Foxp3/Transcription Factor Fixation Buffer. Samples were acquired with a Cytek Aurora (Cytek Biosciences) and analyzed using FlowJo (v10.7.2, BD Biosciences). Statistically significant immune differences were determined by two-way ANOVA with Tukey correction for multiple comparisons. Individual immune populations were graphed separately.

ATAC-seq

mMDSCs and gMDSCs (2–4 million) were sorted from the bone marrow of sham-injected or GL261-implanted male and female mice as described above. The experiment was performed in two biological replicates for each group, and cells from two mice were combined for each replicate. MDSCs were washed with cold PBS and counted on a Countess (Invitrogen). Pellets were resuspended in 1 mL of nuclei permeabilization buffer [PBS with 1 mmol/L dithiothreitol, 5% BSA, 0.2% IGEPAL-CA630 (Sigma Aldrich) and 1× cOmplete EDTA-free protease inhibitor (Roche)] and rotated for 10 minutes at $4°C$ as per the Ren and colleagues protocol (https://www.encodeproject.org/documents/4a2fc974-f021–4f85-ba7a-bd401fe682d1/). The nuclear suspension was filtered on a 30 μm CellTrics (Sysmex) and spun at $500 \times g$ for 5 minutes at $4°C$. The resulting pellet was resuspended in 50 μL tagmentation buffer (33 mmol/L Tris-acetate pH 7.8, 66 mmol/L potassium acetate, 11 mmol/L magnesium acetate, and 16% N'N-dimethylformamide, in water). An aliquot of nuclear suspension was counted on a Countess. For each tagmentation reaction, 160,000 nuclei were mixed with 1 μL of Tagment DNA enzyme in a total of 20 μL and incubated for 30 minutes with 500 rpm at $37°C$. Then 200 μL Buffer PB (Qiagen) and 10 μL sodium acetate (3M, pH 5.2) were added, and the sample was purified using a MinElute PCR Purification Kit (Qiagen) and eluted in 10 μL EB. Fragments were amplified by PCR following the Ren and colleagues protocol but using primers from Buenrostro and colleagues Supplementary Table S1, then purified using the MinElute PCR purification kit with elution in 40 μL EB (15). Size selection was performed with PCRclean Dx beads (ALINE) by adding 160 μL EB to the 40 μL sample and adding 110 μL beads. After mixing and incubation for 5 minutes at room temperature, the tube was put on a magnetic stand and the supernatant transferred to a new tube, to which 190 μL beads was added. This suspension was mixed, incubated, and put on the magnetic stand, and this time the supernatant was discarded. Beads were washed twice with 70% ethanol, then the DNA was eluted from the beads with 20 μL EB. The indexed libraries were sequenced on a NextSeq high-output flowcell, paired-end, 75 cycles.

ATAC-seq data analysis

Cutadapt v1.9.1 (16) was used to remove paired-end adapter sequences and discard reads with a length less than 20bp. All FASTQs were aligned to the mm10 genome assembly (retrieved from http://hgdownload.cse.ucsc.edu/goldenPath/mm10/bigZips) using BWA-MEM v0.7.17-r1188 (17) with default parameters in paired-end mode. Sequence alignment/map (SAM) output files were converted to binary (BAM) format, sorted, indexed, and PCR duplicates were removed using SAMtools v1.10 (18). Peaks were detected with MACS v2.1.2 (19) with –format = BAMPE. DeepTools v3.2.0 (20) was used to generate RPGC-normalized bigWig tracks with 50 bp bin sizes of the final sample BAM files and aggregate bigWig files were generated by averaging the ATAC-seq signals across either all gMSDC or mMSDC samples. Libraries were assessed for quality using ChIPQC (21) and visualized on the Integrative Genomics Viewer (22). Peak lists were filtered to remove all peaks overlapping ENCODE blacklisted regions (mm10 blacklist file v2 downloaded from https://sites.google.com/site/anshulkundaje/projects/blacklists).

Identification of differential open chromatin regions

ATAC-seq peaks called across all samples were filtered for significance [peaks with Benjamini–Hochberg corrected P values (q-val) > 0.001 were excluded], combined together, overlapping peaks merged, and read depth for each peak region across samples determined using BEDTools v2.17.0 (23), generating a count matrix. A total of 43,811 variable regions were detected. Peaks were tested for differential expression by cell type using DESeq2 v1.32.0 (24) after controlling for sex and tumor status and stratifying for peaks with mean normalized counts >50. Differential open chromatin regions were designated as gained or lost by a positive or negative 2-fold change in ATAC signal between mMDSC and gMDSC samples at q value < 0.001.

Gene mapping and ontology analysis

The functional enrichment analysis software Genomic Regions Enrichment of Annotations Tool (GREAT; ref. 25) was used to map genes to peaks and to identify ontology terms associated with differential peaks. The following statistical test thresholds were used to identify significant ontology terms: binomial fold-enrichment >2.0, binomial FDR Q-value < 0.05, and hypergeometric FDR Q-value < 0.05.

Motif analysis

Motif enrichment analysis for gained ATAC-seq peaks was performed using HOMER v4.11 (26) for known transcription factor motifs with the option-size = given against the mm10 genome assembly. Peaks that were neither gained nor lost were used as background regions.

Single-cell expression analysis

Intrastudy normalized matrices of nontumor cells for each of the four studies were downloaded from GigaScience GigaDB database (http://gigadb.org/dataset/100794; ref. 27). Data were combined from four studies containing 50 GBM samples and 9,097 nontumor cells in total. the distribution of samples is as follows: Darmanis and colleagues, GEO accession no. GSE84465, 2498 nontumor cells, $n = 4$ patients, Smart-seq2 technology (28); Yuan and colleagues, GEO accession GSE103224, 4,194 nontumor cells, $n = 10$ patients, proprietary microwell technology (29); Neftel and colleagues, GEO accession GSE131928, 1,067 nontumor cells, $n = 28$ patients, Smart-seq2 technology (30); Yu and colleagues, GEO accession GSE117891, 1,338 nontumor cells, $n = 8$ patients, STRT-seq technology (31). Basic analysis and visualization of the scRNA-seq data were performed with the Seurat R package (v.4.0.2) in R (v.3.3.4). Matrices were processed by SCTransform() and IntegrateData() functions to achieve interstudy normalization and integration (https://satijalab.org/seurat/articles/integration_introduction.html #performing-integration-on-datasets-normalized-with-sctransform-1). The default value was used when running the functions (32, 33). The myeloid cell population was defined based on high ITGAM expression, and subsets were further discriminated on the basis of relative expression profiles of CD84, CD33, ITGAM (CD11b), CD14, OLR1 (LOX-1), CEACAM8 (CD66), and HLA-DR. ATAC-seq gene targets were mapped onto the single-cell-sequencing dataset, and the differentially expressed gene heatmap was generated by Seurat DoHeatmap() function. Cut-off for the gene list was the q value (adj. P; FDR) < 0.05.

Analysis of patient tumors and blood

Five GBM specimens were collected by the Rose Ella Burkhardt Brain Tumor and Neuro-Oncology Center after obtaining written informed consent from the patients. The studies were conducted in

accordance with recognized ethical guidelines and approved by the Cleveland Clinic Institutional Review Board (IRB 2559). Tumors were minced and processed following the instructions for the human tumor dissociation kit (Miltenyi Biotec, 130–095–929). After the addition of enzyme mix in 5 mL null RPMI, samples were digested in a Miltenyi dissociator using the 37_h_TDK_1 program. Cells were treated with RBC Lysis Buffer (BioLegend) at room temperature for 5 minutes. 9 to 10 mL of blood was diluted with 15 mL PBS and laid over 15 mL Cytiva Ficoll-Paque (Thermo Fisher Scientific). Samples were centrifuged at 400 g for 30 minutes with breaks off and the interphase enriched in peripheral blood mononuclear cells were collected. Samples were stained with LIVE/DEAD Fixable Stains for 10 minutes on ice and incubated with FcR Blocking Reagent for 15 minutes on ice. Staining with fluorophore-conjugated CD45, CD33, CD14, CD11c, CD3, CD19, CD56, Lox1, CD11b, CD66, HLA-DR, CD19, CD28 and integrin β7 antibodies was performed in Brilliant Stain Buffer (BD Biosciences) for 20 minutes on ice. Cells were fixed overnight in eBioscience Foxp3/transcription factor fixation buffer. CD68 staining was performed in eBioscience Foxp3/transcription factor permeabilization buffer with 20 minutes of incubation at room temperature. Samples were acquired with a BD LSR Fortessa (BD Biosciences).

Macrophage polarization

Sorted mMDSCs (50,000) were stimulated with 50 ng/mL recombinant mouse M-CSF (BioLegend) in Iscove's modified Dulbecco's medium (IMDM, Media Preparation Core) with 1% Pen/Strep and 20% FBS in the presence of 100 ng/mL anti-integrin β1 blocking antibody for 7 days. Macrophages were removed by Accutase treatment, stained with LIVE/DEAD Fixable Stain for 10 minutes on ice and incubated with FcR Blocking Reagent for 15 minutes on ice. Samples were stained with a cocktail of 1:100 diluted CD68, F4/80, I-A/I-E, CD40, CD206, and PD-L1 antibodies for 20 minutes on ice before analyzing with a BD LSR Fortessa.

T-cell proliferation assay

Splenic CD8+ T cells were isolated from male mice by using CD8a$^+$ T Cell Isolation Kit (Miltenyi Biotec) and following manufacturer's instructions. T cells were stained with 1 μmol/L CFSE (BioLegend) for 5 minutes at 37°C. A total of 100,000 cells were stimulated with anti-CD3/CD28 Dynabeads (Thermo Fisher Scientific) plus 50 ng/mL mIL-2 (BioLegend) in the presence or absence of 100 μmol/L sitagliptin. Samples were analyzed using a BD LSR Fortessa on Day 5.

qRT-PCR

RNA was isolated from sorted mMDSCs and gMDSCs using the Qiagen RNeasy Mini Kit, and the concentration was measured with a NanoDrop 2000 (Thermo Fisher Scientific). cDNA was synthesized using qScript cDNA Supermix (Quanta Biosciences) in a thermal cycler (Eppendorf). qPCR reactions were performed using a QuantStudio3 (Thermo Fisher Scientific) and Fast SYBR-Green Mastermix (Thermo Fisher Scientific). For qPCR analysis, the threshold cycle (Ct) values for DPP-4 were normalized to the expression levels of Actin. See primers (Eurofins) used in **Table 1**.

Table 1. Primers (Eurofins) used.

Dpp-4:	Forward: 5′-GACTCTCTCAGCTCATCCTCTA-3′
	Reverse: 5′-GCCCACACCACATCACATAA-3′
Actin:	Forward: 5′-GGCTGTATTCCCCTCCATCG-3′
	Reverse: 5′-CCAGTTGGTAACAATGCCATGT-3′

Intracellular staining

A total of 250,000 to 500,000 sorted mMDSCs and gMDSCs was cultured overnight in 10% RPMI supplemented with 50 ng/mL GM-CSF and IL13 (BioLegend) in 24-well plates (Corning Costar) and treated with 100 μg/mL sitagliptin. A fraction of the cells was stained with 1:1,000 diluted Draq 7 (Thermo Fisher Scientific) in PBS for 10 minutes at room temperature to assess viability using a BD LSR Fortessa. The remaining cells were incubated with 1.5% paraformaldehyde (Thermo Fisher Scientific) and 1× eBioscience Foxp3/transcription factor permeabilization buffer for 20 minutes at room temperature. Samples were stained with 1:50 diluted phospho-Akt (Ser473; D9E) XP Rabbit mAb (Alexa Fluor 647 Conjugate; Cell Signaling Technology, 4075S), phospho-p44/42 MAPK (ERK1/2; Thr202/Tyr204; E10) Mouse mAb (Alexa Fluor 647 Conjugate; Cell Signaling Technology, 4375S), or rabbit IgG Isotype Control (Alexa Fluor 647 Conjugate; Cell Signaling Technology, 3452S) in 1× eBioscience Foxp3/transcription factor permeabilization buffer for 1 hour at room temperature. Samples were acquired with a Cytek Aurora.

Transwell assay

A total of 100,000 GL261, GL261-GFP, or SB28 cells were seeded on the bottom chamber in 500 μL 10% RPMI and treated with 100 μg/mL sitagliptin. Sorted mMDSCs and gMDSCs were stained with 1:1,000 diluted CellTrace Violet (Thermo Fisher Scientific) in PBS for 15 minutes at 37°C. mMDSCs and gMDSCs (200,000–250,000) were added on the top chamber of a 24-well plate with a 5.0 μm polycarbonate membrane (Costar) in 100 μL 10% RPMI containing 100 μg/mL sitagliptin. Cells from bottom and top chambers were collected the next day, and samples were acquired with a BD LSR Fortessa. Migration frequency was determined by the bottom cell #/(bottom cell # + top cell #).

Cancer cell viability

A total of 1,000 GL261 and SB28 cells were plated into 96-well white-walled plates (Thermo Fisher Scientific) in 100 μL 10% RPMI and treated with 100 μg/mL sitagliptin overnight. ATP levels were measured on a Victor Nivo Multimode Microplate Reader (PerkinElmer) using CellTiter-Glo Luminescent Cell Viability Assay (Promega).

Statistical analysis

GraphPad PRISM (Version 9, GraphPad Software Inc.) software was used for data presentation and statistical analysis. Two-way ANOVA, one-way ANOVA, unpaired t tests, and paired t tests were used for comparison of differences among sample groups. The Gehan–Breslow–Wilcoxon test was used to analyze survival data. The specific statistical method employed for individual data sets is listed in the figure legends.

Data availability

The data generated in this study are publicly available in Gene Expression Omnibus (GEO) at GSE206551.

Results

mMDSCs but not gMDSCs drive GBM upon adoptive transfer

We previously demonstrated that mMDSCs accumulated during the advanced stages of GBM progression in preclinical models and that targeting of mMDSCs but not gMDSCs with nonspecific inhibitors prolonged survival of male mice with GBM (12). To more directly
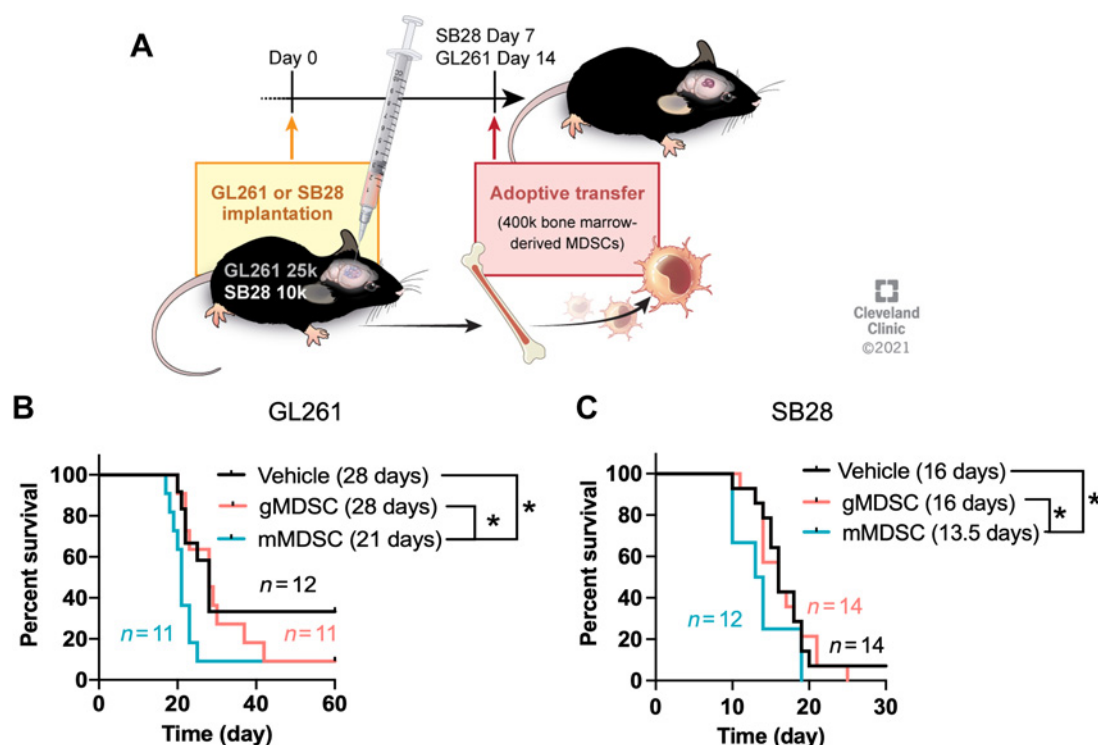
Figure 1.
mMDSCs but not gMDSCs promote tumor growth. **A,** Male C57BL/6 mice were implanted with 25,000 GL261 or 10,000 SB28 cells. Seven (SB28) or 14 (GL261) days posttumor implantation, mice were adoptively transferred with 400,000 mMDSCs or gMDSCs isolated from the bone marrow of male mice with matching tumors by retro-orbital injection. **B** and **C,** Kaplan–Meier curves depicting survival of GL261- (**B**) or SB28-bearing (**C**) mice post-adoptive transfer. $n = 11$–14 mice/group from three independent experiments. *, $P < 0.05$ as assessed by Wilcoxon-rank test.

interrogate the tumorigenic effects of MDSC subsets on tumor growth, we implanted male mice with syngeneic mouse tumor models (GL261 and SB28), before adoptively transferring bone marrow-derived mMDSCs or gMDSCs at a time point when there is no significant mMDSC accumulation (**Fig. 1A**, data not shown). The transfer of male mMDSCs reduced the median survival duration by 15% to 25% in both models, whereas male gMDSCs had no impact on the median survival (**Fig. 1B** and **C**). To eliminate the possibility that the lack of change in tumor latency post-gMDSC adoptive transfer is due to reduced retention of this subset, we adoptively transferred two fold more gMDSCs and observed no significant differences in tumorigenesis (Supplementary Figs. S1A and S1B). We previously reported sex differences in MDSC subset activity in GBM, with increased tumor-infiltration of male mMDSCs in animal models and patients with GBM (12). Thus, to further explore whether the tumor-promoting effect of mMDSCs was informed by the sex of the cells, we repeated the adoptive transfer experiments using MDSCs isolated from female hosts and observed a similar trend, with mMDSCs accelerating tumorigenesis and gMDSCs having no effect on the course of GBM progression (Supplementary Figs. S1C and S1D). Collectively, these results suggest that mMDSCs inherently drive progression of GBM in preclinical models to a greater extent than gMDSCs, which show equivalent malignancy to vehicle controls.

mMDSCs and gMDSCs have distinct chromatin accessibility signatures

Several studies have identified unique gene expression signatures associated with MDSC subsets in mouse cancer models and patients

with malignancies (12, 34–36). However, the epigenetic basis underlying distinct MDSC characteristics and expression profiles remain unclear. Therefore, we performed ATAC-seq on mMDSCs and gMDSCs isolated from the bone marrow of GL261-bearing or control male and female mice (**Fig. 2A**). Unsupervised clustering analyses revealed no significant differences between the chromatin accessibility of MDSCs obtained from sham-injected versus GL261-injected mice, suggesting that these cells do not undergo major developmental reprogramming in bone marrow in the presence of tumors (**Fig. 2B**). In addition, in MDSCs isolated from sham-injected control and tumor-bearing mice, 25% to 28% of the variance in genome-wide accessibility was linked to host sex, whereas subtype identity accounted for 70% to 73%, further underscoring the role of cellular identity as the main determinant of the epigenetic architecture of MDSC subsets (**Fig. 2C**; Supplementary Figs. S2A and S2B). Therefore, we focused on the differentially accessible regions between mMDSCs and gMDSCs by controlling for sex and tumor state. This approach identified a total of >40,000 variable locations (**Fig. 2D**), of which, 12,613 (29%) were gained and 7,929 (18%) were lost peaks in mMDSCs. Of note, 70.4% of the gained peaks were conserved between mMDSCs from control versus tumor-bearing mice, pointing to the presence of core epigenetic programming in mMDSCs (Supplementary Fig. S2C). We next performed gene ontology analysis using the peaks gained in mMDSCs to evaluate whether genes localized at these more accessible regions are enriched in specific pathways. This approach revealed a 177-gene "regulation of leukocyte cell-cell adhesion" signature as the top pathway associated with mMDSCs over gMDSCs (**Fig. 2E**; Supplementary
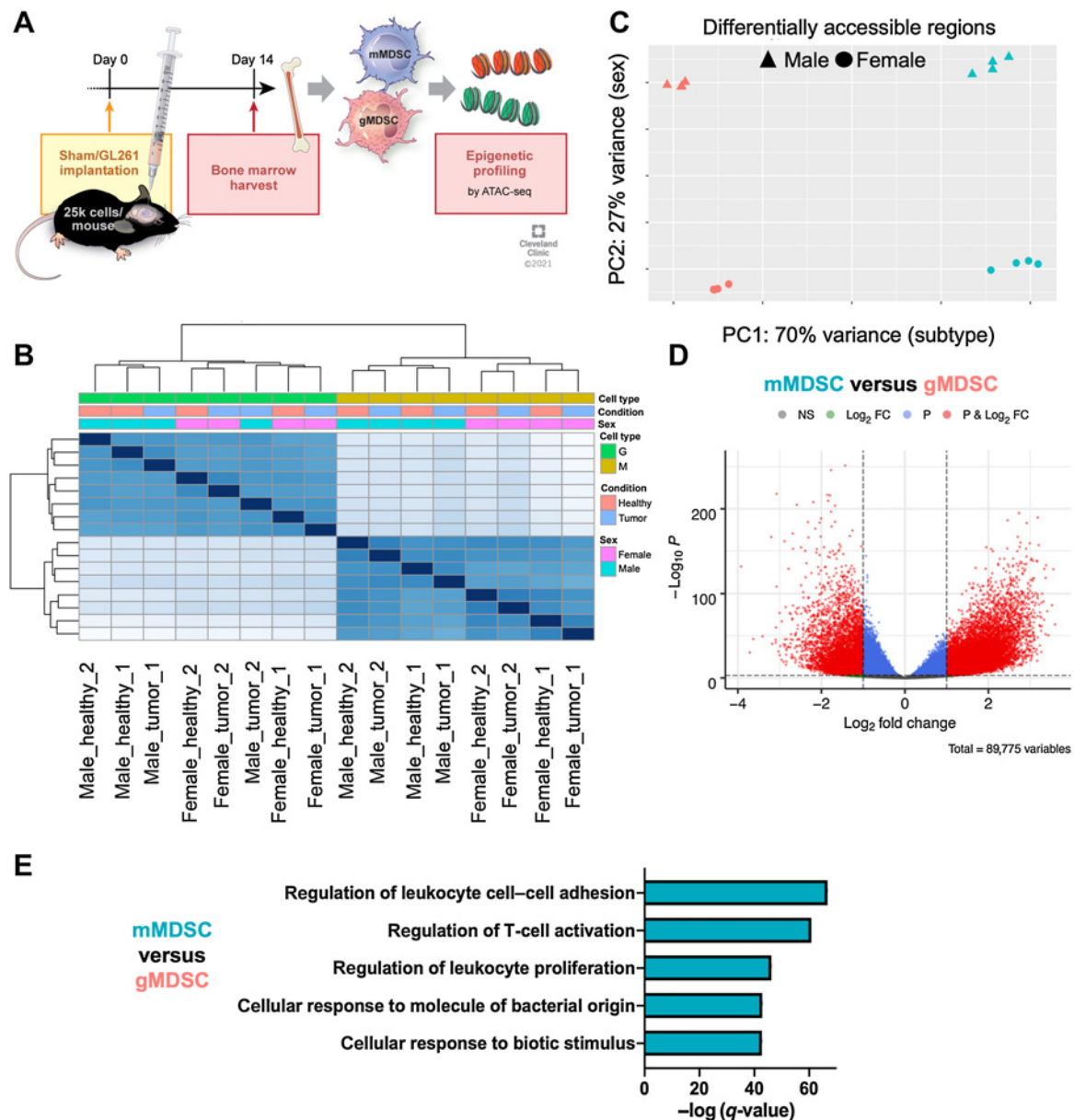
Figure 2.
mMDSCs and gMDSCs have distinct epigenetic programming. **A,** C57BL/6 mice were implanted with 25,000 (male) and 30,000 (female) GL261 cells or were sham injected. Fourteen days later, mMDSCs or gMDSCs were isolated from the bone marrow for ATAC-seq. **B,** Clustering analysis demonstrating the impact of cell type, tumor type, and sex on chromatin accessibility profile. Count data for the sample set were normalized for library size and variance stabilized using DESeq2's regularized log (rlog) transform, then clustered using a Euclidean distance metric. **C,** Principal component analysis (PCA) on rlog-transformed count data for all accessible chromatin regions across samples depicting the relative contribution of cell type (major) and sex (minor) on chromatin accessibility. **D,** Differentially accessible open chromatin regions between mMDSCs and gMDSCs with peak count >50 determined with DESeq2 and controlled based on tumor state and sex. Differential open chromatin regions were designated as gained or lost by a positive or negative two-fold change in ATAC signal between mMDSC and gMDSC samples at $P_{adj} < 0.001$–43,811 variable regions were found. **E,** Program GREAT was used to identify the top 5 pathways upregulated in mMDSCs with log_2-fold change ≥1 and adjusted $P ≤ 0.001$ based on the gained peaks in mMDSCs.

Fig. S2D; Supplementary Table S1). To further identify whether there are master regulators potentially controlling the expression of cell adhesion-related genes in mMDSCs, we performed motif analysis on gained peaks and identified PU.1 and IRF8, a negative regulator of gMDSC commitment (35, 37, 38), as potential transcription factors driving this signaling axis (Supplementary Table S2).

Integrin β1 is highly expressed in mouse and human mMDSCs

Enhanced adhesion is a common feature of malignant tumors and is linked to chemotaxis and tumor infiltration of immune cells (39). As integrins are a major class of receptors that recognize multiple extracellular matrix (ECM) proteins and are essential for adhesion and downstream signaling (40), we focused on the potential link

between integrins and the elevated adhesion signature in mMDSCs. Integrins are heterodimers formed by interaction of α- and β-chains and show variable expression across cell populations, with integrins β1, β2, and β7 playing a central role in leukocyte migration (39, 40). However, there is limited knowledge on the differential integrin expression profile of MDSC subsets and how it is linked to their behavior. ATAC-seq analysis revealed that *Itgb1, Itgb2,* and *Itgb7* contained open-chromatin regions, highlighting the potential for gene transcription in mMDSCs and gMDSCs (**Fig. 3A**). Analysis of surface integrin β1, β2, and β7 subunits in mice with GL261 or SB28 tumors and sham-injected controls demonstrated that myeloid cells in circulation and in tumors had higher levels of integrins β1 and β7 compared with lymphocytes (Supplementary Figs. S3A and S3B, data not shown). Although integrin β2 levels were also higher in blood myeloid popula-

tions, tumor-infiltrating adaptive immune cells upregulated this receptor (Supplementary Fig. S3B). A pairwise comparison of the receptor expression on mMDSCs versus gMDSCs showed that mMDSCs had significantly more surface integrins in the bone marrow of tumor-bearing and healthy mice (**Fig. 3B**). Although this pattern was retained for integrins β1 and β7 in blood and tumors, gMDSCs in these compartments had similar or higher levels of integrin β2 compared with mMDSCs (**Fig. 3C** and **D**). We also stained the cells with antibody clone Huts-4, which specifically recognizes the active conformation of integrin β1, and detected significantly higher levels of activated integrin β1 in circulating mMDSCs compared with gMDSCs (Supplementary Fig. S3C). Importantly, there were no significant differences in integrin levels between male and female mMDSCs, supporting the observation that epigenetic regulation is primarily
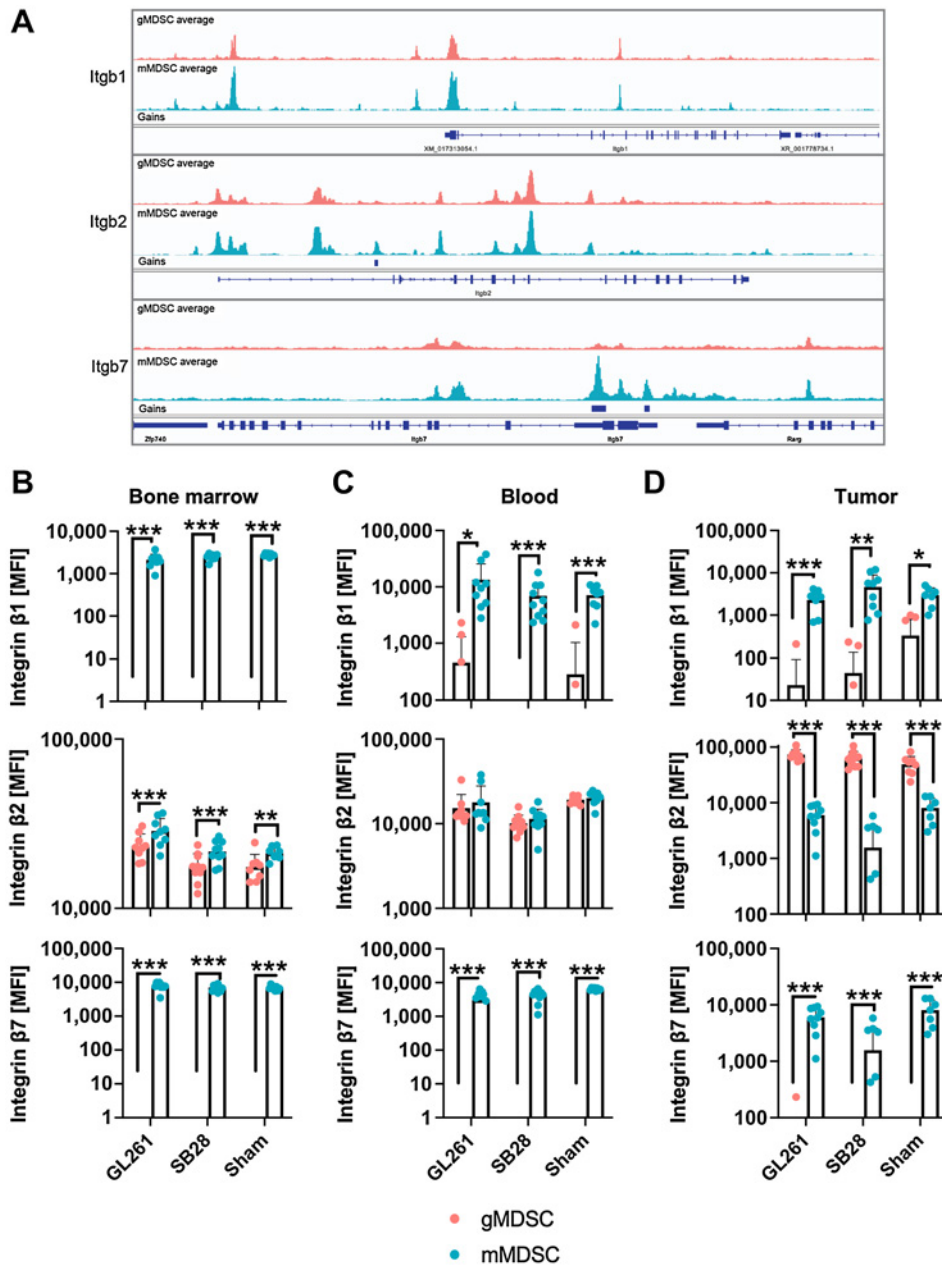

Figure 3.
Mouse mMDSCs consistently express higher levels of integrin β1. **A,** Cross-section of integrin β1 (*Itgb1*), integrin β2 (*Itgb2*), and integrin β7 (*Itgb7*) loci demonstrating gained peaks in mMDSCs and gMDSCs as assessed by ATAC-seq. C57BL/6 mice were implanted with 25,000 GL261 cells and 15,000 SB28 cells or sham injected. Mice were euthanized 12 (SB28) or 19 (GL261) days posttumor implantation. **B–D,** Differential expression of surface integrin β subunits by mouse mMDSCs and gMDSCs localized at bone marrow (**B**), blood (**C**), and tumors/brains (**D**). *, $P < 0.05$; **, $P < 0.01$; ***, $P < 0.001$ by two-way ANOVA.
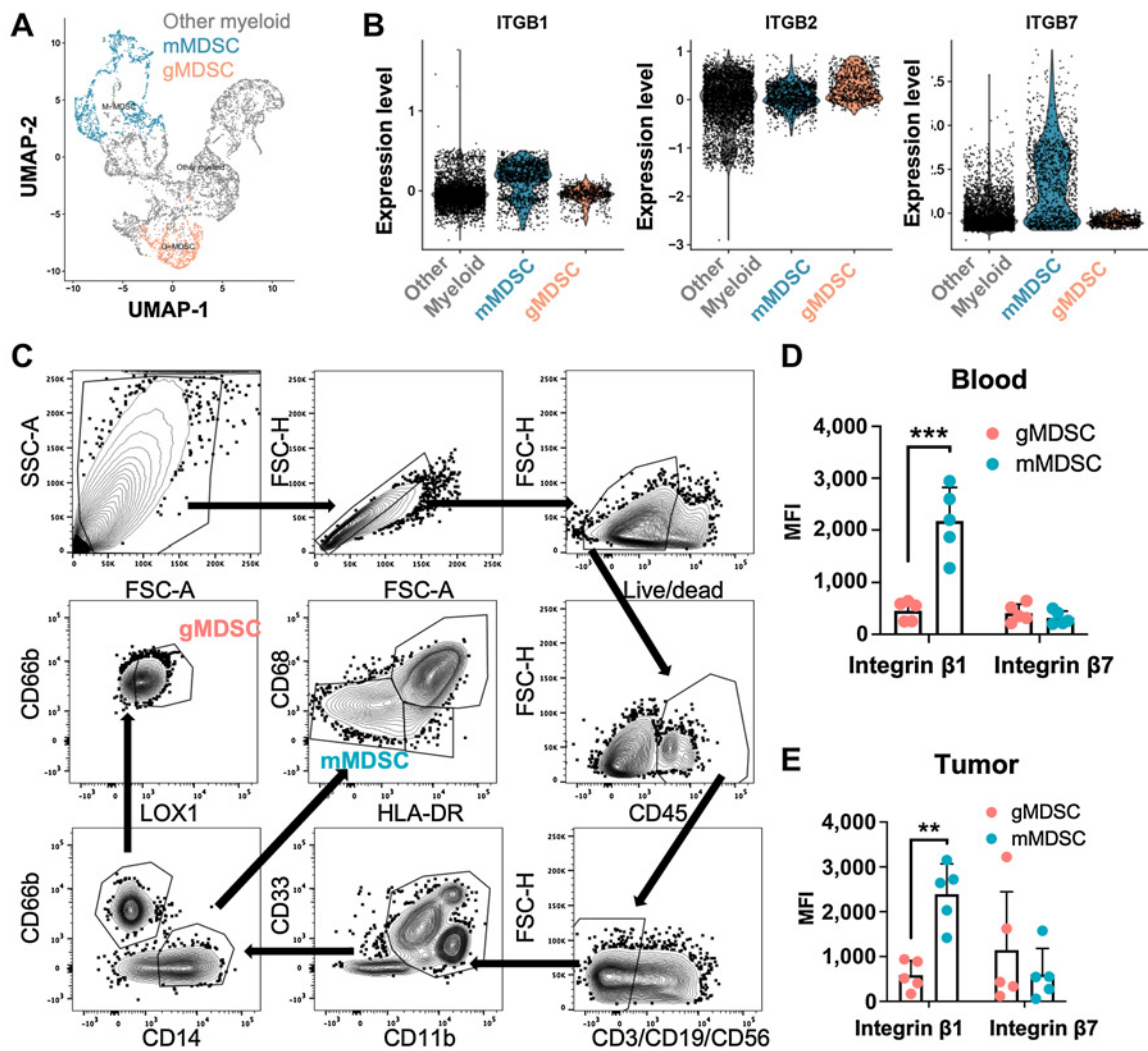
Figure 4.
Patient mMDSCs have increased integrin β1 expression. **A,** Uniform manifold approximation and projection (UMAP) plots depicting distribution of myeloid cell subpopulations in patient tumors defined on the basis of markers given in Supplementary Figs. S3A–S3B. $n = 50$ combined from Darmanis and colleagues (28). **B,** Expression levels of integrin *β1, β2,* and *β7* in tumor myeloid cells at a single-cell resolution in myeloid cell populations. **C,** Representative histograms demonstrating gating of mMDSC and gMDSC populations in blood and tumor of patients with GBM. **D** and **E,** Surface integrin β1 and β7 expression on human mMDSCs and gMDSCs from blood (**D**) or tumors [$n = 5$ (2 male, 3 female); **E**]. **, $P < 0.01$; ***, $P < 0.001$ by two-way ANOVA. MFI, mean fluorescence intensity.

influenced by cell identity (**Fig. 2C**; Supplementary Figs. S2A, S2B, S3D, and S2B). To further validate these observations in patients with GBM, we analyzed single-cell expression profiles of integrin β1 (*ITGB1*), β2 (*ITGB2*), and β7 (*ITGB7*) in tumor-infiltrating mMDSCs and gMDSCs using publicly available datasets (27). The myeloid lineage was initially defined based on *ITGAM* expression and was reclustered to distinguish mMDSCs and gMDSCs from other myeloid cells based on differential expression levels of *CD84, CD33, ITGAM (CD11b), CD14, OLR1 (LOX-1), CEACAM8 (CD66),* and *HLA-DR* (**Fig. 4A**; Supplementary Figs. S4A and S4B). A comparison between these two cell populations demonstrated that mMDSCs expressed higher levels of *ITGB1* and *ITGB7* but not *ITGB2* compared with gMDSCs (**Fig. 4B**). We sought to confirm the correlation between RNA and protein levels by measuring surface integrin β1 and β7 levels in patient specimens (**Fig. 4C**). mMDSCs circulating in the blood or localizing to tumors had significantly more integrin β1 compared with

gMDSCs, whereas integrin β7 intensity was similar between the two subsets (**Fig. 4D** and **E**; Supplementary Fig. S4C). Myeloid-dominant and consistent expression of integrin β1 in the bone marrow, blood and tumor suggests that integrin β1 is a putative target to regulate immunosuppression in GBM.

Blockade of integrin β1 abrogates mMDSC function

To evaluate the impact of mMDSC-specific targeting of integrin β1, we pretreated sorted donor cells with an anti-integrin β1 neutralizing (anti-β1) or control isotype antibody *in vitro* prior to adoptive transfer. Mice that received mMDSCs incubated with anti-β1 antibody had significantly longer tumor latency compared with mice receiving mMDSCs pretreated with isotype control antibody ($P < 0.05$, **Fig. 5A**). These data indicate that integrin β1 blockade abrogates the tumor-promoting role of these cells. Of note, these differences are likely not due to the induction of MDSC cell death, as we observed no significant difference in cell viability during the
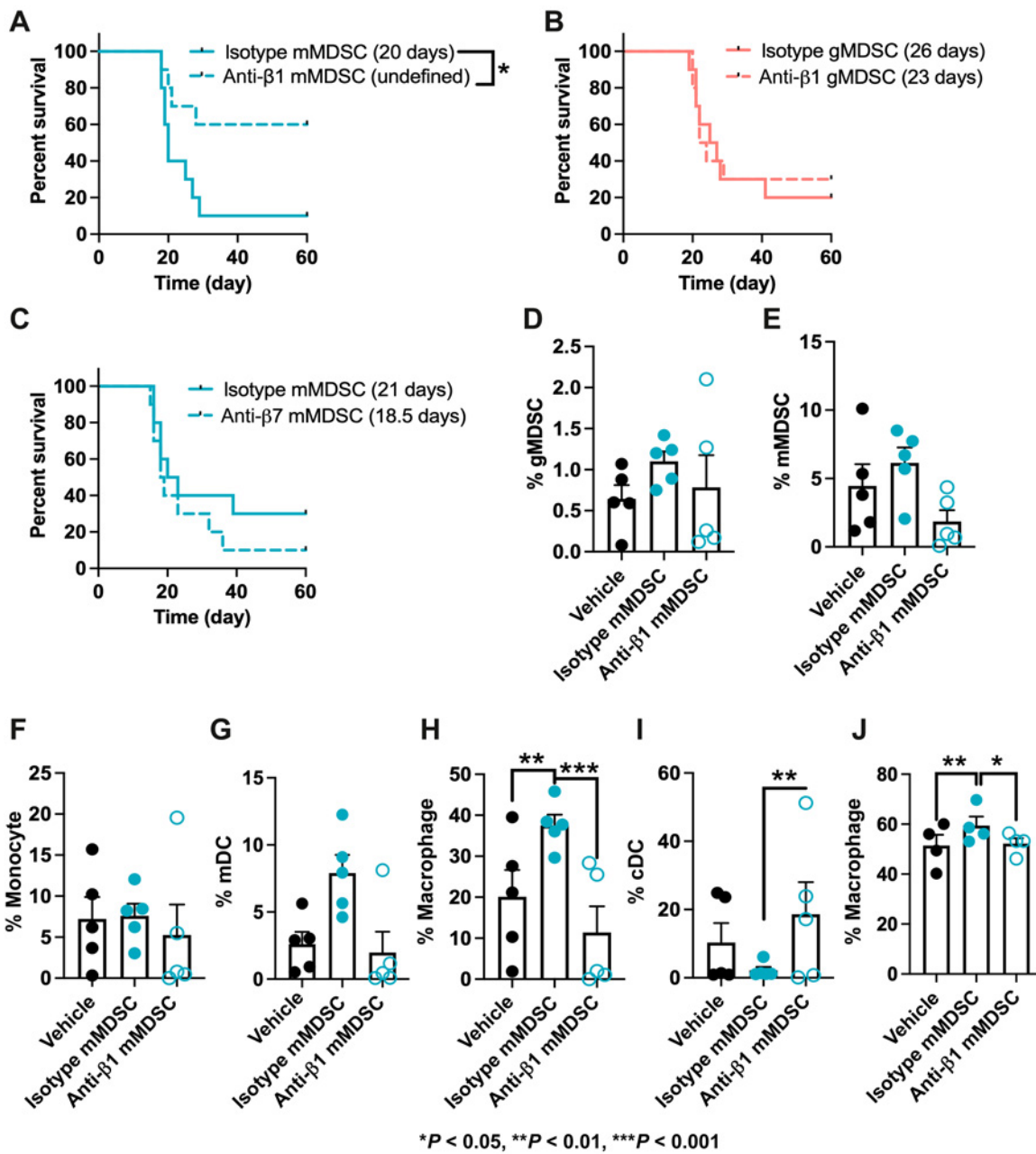
Figure 5.
Integrin β1 comprises a therapeutic target to regulate mMDSC function. Bone marrow–derived male mMDSCs and gMDSCs were treated with 100 µg/mL anti-integrin β1, anti-integrin β7, or isotype control antibody prior to adoptive transfer. **A–C,** Kaplan–Meier plot depicting survival of GL261-bearing male mice transferred with mMDSCs treated with anti-integrin β1 neutralizing antibody (**A**), gMDSCs treated with anti-integrin β1 neutralizing antibody (**B**), or mMDSCs treated with anti-integrin β7 neutralizing antibody (**C**) compared with isotype control. $n = 9$–10 from two independent experiments. *, $P < 0.05$ as assessed by Wilcoxon-rank test. C57BL/6 male mice were implanted with 25,000 GL261 cells and adoptively transferred on Day 7 with 400,000 mMDSCs treated with isotype control antibody or anti-integrin β1 blocking antibody for 1 hour. Myeloid cell populations were analyzed from tumors 3 days later. The frequency of tumor-infiltrating gMDSCs (**D**), mMDSCs (**E**), monocytes (**F**), macrophages (**G**), myeloid DCs (**H**), and conventional DCs (**I**) in mice adoptively transferred with isotype- or anti-integrin β1-treated mMDSCs ($n = 5$/group). Only significant differences are shown in the figure. C57BL/6 male mice were implanted with 15,000 SB28 cells and adoptively transferred with 400,000 mMDSCs treated with isotype control antibody or anti-integrin β1 blocking antibody for 1 hour on Day 4. Myeloid cell populations were analyzed from tumors 3 days later. **J,** The frequency of tumor-infiltrating macrophages in mice adoptively transferred with isotype- or anti-integrin β1-treated mMDSCs ($n = 4$/group). *, $P < 0.05$; **, $P < 0.01$; ***, $P < 0.001$ as determined by two-way ANOVA with Tukey correction.

1 hour antibody incubation (data not shown). As expected, transfer of donor gMDSCs stimulated with an anti-β1 antibody had no effect on the median survival duration of mice with tumors (**Fig. 5B**). To further assess the specificity of integrin β1 signaling, we repeated the same experiment while instead blocking integrin β7 on mMDSCs. There was no significant difference between the survival span of mice that acquired isotype-treated versus anti-β7-treated mMDSCs (**Fig. 5C**). On the basis of this observation that integrin β1 inhibition selectively alters mMDSC function, we focused on the mMDSC-related changes in the tumor microenvironment. GL261-bearing mice were adoptively transferred with mMDSCs and gMDSCs with intact or blocked surface integrin β1, and the frequency of circulating and tumor-infiltrating immune populations was analyzed 3 days later. Overall, leukocyte infiltration, as well as the relative frequency of mMDSC, gMDSCs, monocytes, myeloid DCs, B cells CD4$^+$ T cells, CD8$^+$ T cells, and NK cells, was similar between the isotype and anti-β1 groups (**Fig. 5D–G**; Supplementary Figs. S5A and S5B). In contrast, there was a significant increase in the abundance of macrophages with a concomitant reduction in conventional dendritic cell (cDC) frequency in mice with isotype-treated mMDSCs (**Fig. 5H** and **I**). A similar change in the frequency of macrophages was also observed in the SB28 model (**Fig. 5J**). Importantly, the observed immune changes were limited to the tumor microenvironment and specifically induced by mMDSCs, as gMDSC transfer did not alter the frequency of various innate or adaptive cells in GL261 tumors and there were significant variations in peripheral immune populations (Supplementary Figs. S5C and S5D). Thus, the enhanced macrophage abundance could be a result of mMDSC differentiation into tumor-associated macrophages (41, 42) or an indirect consequence of the interaction between mMDSCs and macrophages, leading to an accumulation of the latter population (43). Blockade of integrin β1 *in vitro* did not interfere with mMDSC-to-macrophage differentiation or the phenotype of macrophages (Supplementary Figs. S5E and S5F), indicating that the observed changes may not be a consequence of direct blockade of polarization.

DPP-4 inhibition alters mMDSC behavior and the tumor immune microenvironment

We next sought to investigate the potential of the integrin β1-related cell adhesion signature as a translational target in GBM as broad expression profile of integrin β1 could be a limiting factor. Mapping of ATAC-seq gene targets (Supplementary Table S1) to a patient single-cell sequencing dataset demonstrated that 24 genes with increased accessibility in mouse mMDSCs were expressed at significantly higher rates in tumor-infiltrating human mMDSCs compared with gMDSCs (**Fig. 6A**). Among the top hits, DPP-4 was previously identified as an interacting partner of integrin β1 (**Fig. 6A**; Supplementary Fig. S6A; ref. 44). Consistent with the enhanced accessibility profile of the *Dpp-4* locus, this gene was expressed ~7-fold more highly in mouse mMDSCs compared with gMDSCs (**Fig. 6B** and **C**). Thus, we used this model system to evaluate the potential role of DPP-4 in MDSC function using the clinically approved inhibitor sitagliptin. Assessment of migratory potential with transwell assays demonstrated that mMDSCs preferentially moved toward SB28 cells over GL261 cells, whereas gMDSCs did not exhibit directed migration toward the tumor cells (Supplementary Fig. S6B). The addition of sitagliptin in this setting significantly reduced the migration of mMDSCs to SB28 cells without impacting the behavior of gMDSCs (**Fig. 6D**). Importantly, this effect was not a consequence of reduced cell viability, as sitagliptin did not significantly affect the survival of either MDSC subsets or tumor cells (Supplementary Figs. S6C and S6D). To further investigate the intracellular signaling networks involved in differential DPP-4 activity, we treated MDSC subsets overnight with sitagliptin in the

presence of prosurvival cytokines. mMDSCs had significantly higher levels of phosphorylated ERK (pERK) signaling compared with gMDSCs, whereas pAkt levels were not different between the two cell populations (**Fig. 6E**; Supplementary Figs. S6E and S6F). Correspondingly, blockade of DPP-4 resulted in a decline in pERK levels specifically in mMDSCs but not gMDSCs, whereas pAkt levels remained unchanged (**Fig. 6F**; Supplementary Fig. S6G). We next interrogated the effect of DPP-4 inhibition *in vivo* by treating GL261- and SB28-bearing immunocompetent C57BL/6 mice with sitagliptin. For both tumor models, there was a significant elongation in the survival duration of mice that received sitagliptin compared with vehicle control (**Fig. 6G**; Supplementary Fig. S6H). However, this effect on survival was not observed in immunocompromised NSG mice, suggesting that sitagliptin modulates antitumor immune response (Supplementary Figs. S6I and S6J). Further analysis of potential immunologic changes was carried out when the first animal presented with disease symptoms. In two separate experiments, we observed that the frequency of CD45$^+$ cells was reduced in GL261-bearing mice treated with sitagliptin (**Fig. 6H**). This effect was primarily driven by a decrease in the abundance of the tumor-associated macrophage population rather than changes in the frequency of other innate and lymphoid cell lineages or activation of intratumoral CD8$^+$ T cells (**Fig. 6I**; Supplementary Figs. S6K and S6L). Collectively, these results demonstrate that integrin β1 and related DPP-4 signaling contribute to mMDSC function in GBM and highlight the potential of cell adhesion programming as a therapeutic target (**Fig. 7**).

Discussion

Despite recent advancements in the field of immuno-oncology, immunotherapies, in particular checkpoint inhibitors, have had limited impact on improving the outcome of GBM (45). These clinical experiences underscore the potential role of immunosuppressive myeloid cells, including MDSCs, in driving treatment resistance and their value as next-generation immunotherapy targets. Thus, there is pressing need to better understand the regulatory mechanisms that drive generation, chemotaxis, and function of immunosuppressive myeloid cells.

We previously reported that mMDSCs were the predominant MDSC subset in the GBM microenvironment and that their non-specific targeting with chemotherapeutics can extend survival in preclinical models (12). Building on this observation, our current results establish that mMDSCs can directly promote tumorigenesis. Despite considerable differences in their mutational burden and response to checkpoint inhibitors, GL261 and SB28 tumors are both heavily infiltrated by myeloid cell populations (12, 46). Consistently, we observed that both GL261- and SB28-bearing mice adoptively transferred with mMDSCs succumbed to GBM earlier or treated with pharmaceutical inhibitor survived longer. However, the magnitude of effect was more limited in SB28 compared with GL261, correlating with enhanced aggressiveness, higher percentage of tumor-infiltrating myeloid cells and short latency of this tumor type. This observation further underscores the importance of myeloid cells and in particular mMDSCs in driving disease progression in distinct tumor environments.

Earlier studies have established that mMDSCs and gMDSCs have unique transcriptional profiles and undertake differential roles in tumors (11, 34–36), but very little is known about the cell-intrinsic molecular determinants of MDSC subset-specific characteristics. We hypothesized that the disease-accelerating phenotype of mMDSCs over gMDSCs is linked to their omics. To address this knowledge gap,
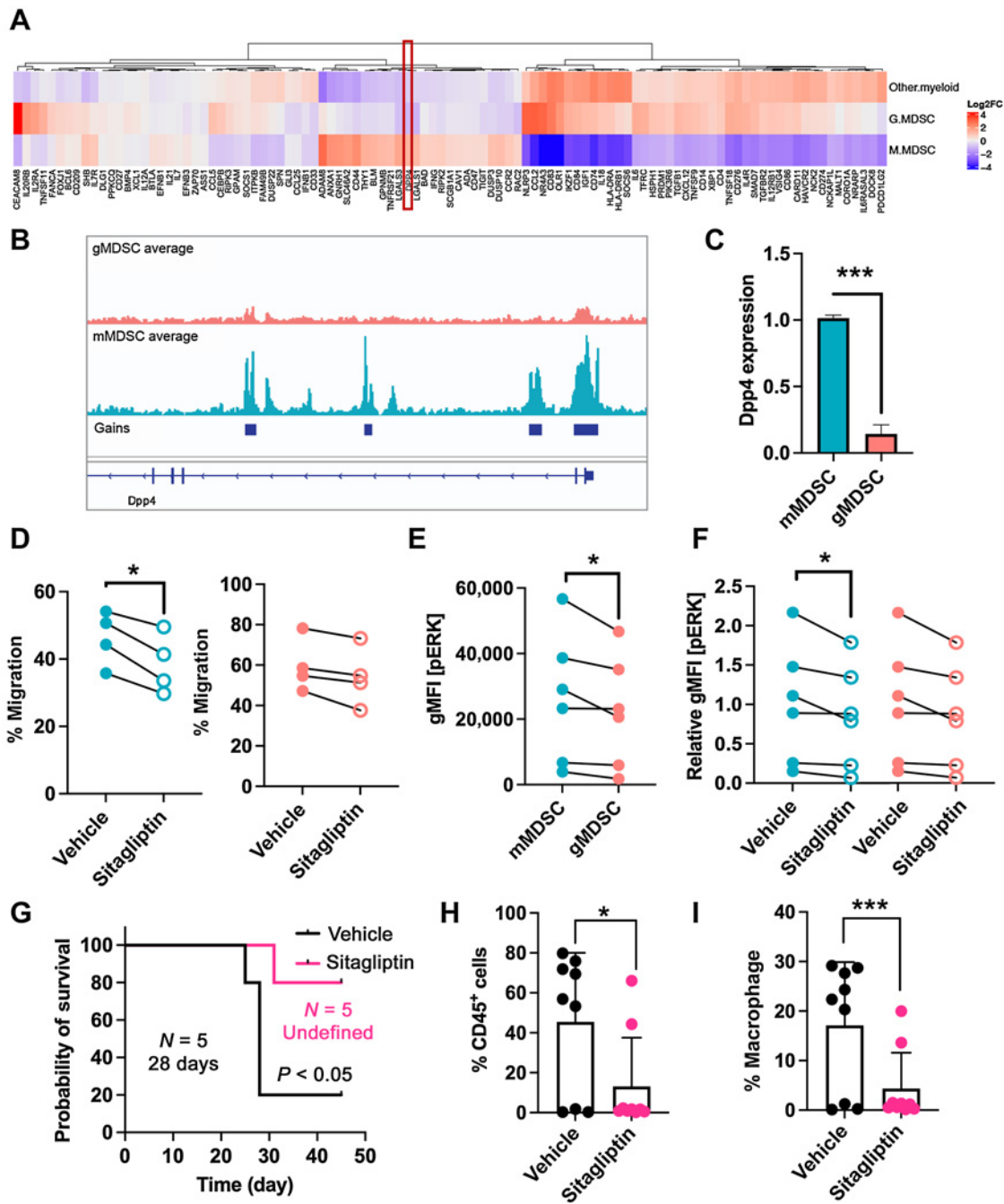
Figure 6.
DPP-4 inhibition targets mMDSC activity and extends survival in GBM. **A,** Differential expression levels of ATAC-seq gene targets in human mMDSC and gMDSC populations defined at the single-cell sequencing dataset. **B,** Gained peaks at the *Dpp-4* locus in mouse mMDSCs compared with gMDSCs. **C,** Relative expression of *Dpp-4* in bone marrow–derived mMDSCs and gMDSCs [$n = 4$ (2 males and 2 females). ***, $P < 0.001$ as assessed by paired t test. **D,** A total of 100,000 SB28 cells were cultured in 24-well plates, and 250,000 CellTrace Violet–stained mMDSCs (left) or gMDSCs (right) were added on the top chamber with a 5 μm pore size. Cell migration was measured after overnight incubation with 100 μg/mL sitagliptin ($n = 5$). *, $P < 0.05$ as assessed by paired t test. **E,** Geometric mean fluorescence intensity (gMFI) of pERK signaling in mMDSCs versus gMDSCs treated with 50 ng/mL GM-CSF and IL13 overnight ($n = 6$). *, $P < 0.05$ as assessed by paired t test. **F,** mMDSCs (left) and gMDSCs (right) were stimulated overnight with 50 ng/mL GM-CSF and IL13 in the presence of 100 μg/mL sitagliptin. Relative intensity of pERK was detected by intracellular staining and flow cytometry ($n = 6$). *, $P < 0.05$ as assessed by paired t test. **G,** C57BL/6 mice were intracranially implanted with 25,000 GL261 cells, and mice were intraperitoneally injected with 25 mg/kg sitagliptin. Kaplan–Meier curves depicting survival of GL261-bearing mice treated with sitagliptin versus vehicle control ($n = 5$/group). **H,** Percentage of CD45$^+$ cells in GL261 tumors treated with sitagliptin or vehicle control ($n = 9$ from two independent experiments). *, $P < 0.05$ as assessed by paired t test. **I,** Abundance of macrophages in GL261 tumors treated with sitagliptin or vehicle control shown as percentage of the live population ($n = 9$ from two independent experiments). ***, $P < 0.001$ as assessed by two-way ANOVA.

Figure 7.
mMDSCs express higher levels of integrin β1 and DPP4, and their targeting reduces tumor-associated macrophage abundance. Reprinted with permission, Cleveland Clinic Foundation ©2022. All Rights Reserved.
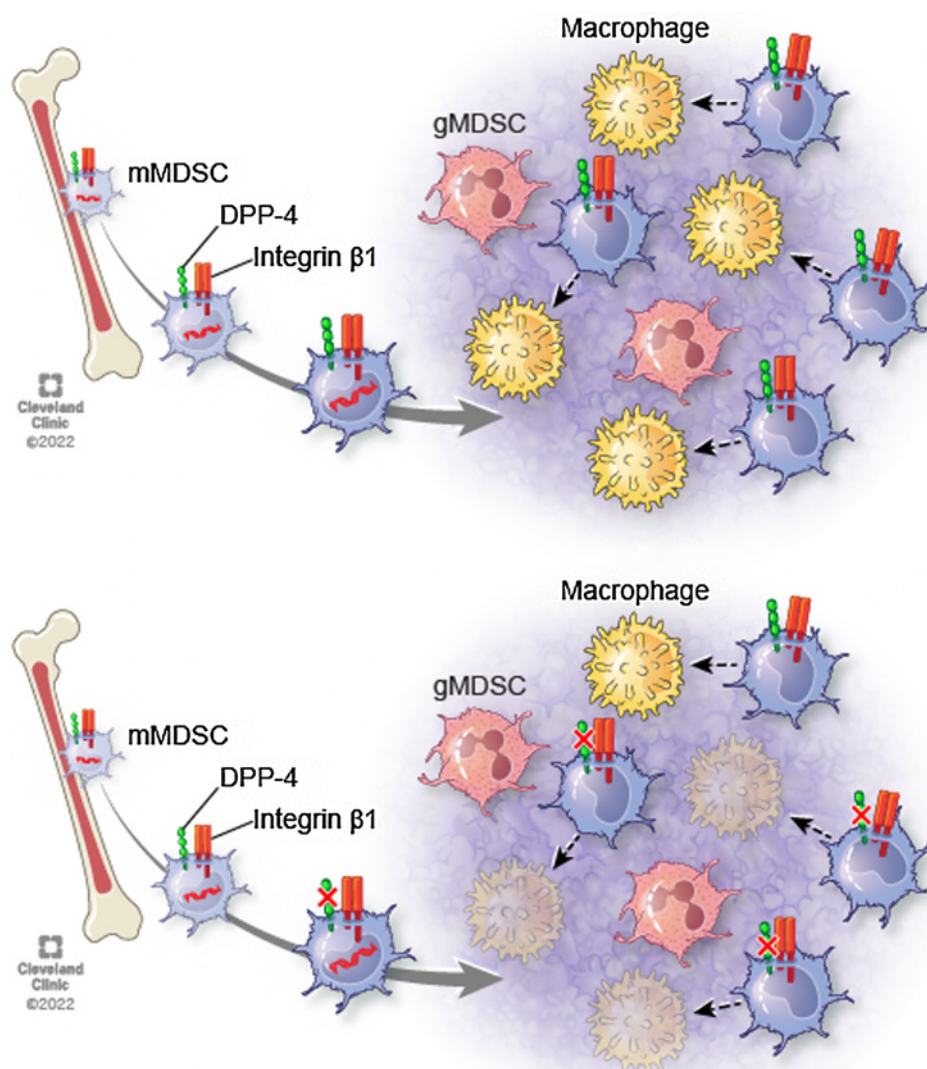
we used ATAC-seq to identify mechanisms driving the distinct behavior of MDSC subsets and identified more than 40,000 differentially accessible regions between mMDSCs and gMDSCs regardless of whether these cells were derived from tumor-bearing hosts at early stages of the disease or healthy control mice. Our analysis demonstrated that IRF8-binding motifs were enriched in peak regions gained in the mMDSC population, suggesting that these regions are more susceptible to IRF8-driven transcription. This is of particular importance as downregulation of IRF8 transcriptional profile is essential for the commitment of granulocyte progenitors that give rise to gMDSCs, whereas high IRF8 levels are required for the development of monocyte-DC progenitors that can differentiate into mMDSCs (35, 37, 38). Therefore, these observations point to a potential link between epigenetic landscape and core transcriptional programs that drive lineage commitment of MDSC subsets and highlight the potential of targeting key molecular mechanisms to modulate MDSC activity. Our results established that cell adhesion is one such pathway, as cell adhesion-related genes were more accessible in mMDSCs compared with gMDSCs. This is consistent with two recent studies demonstrating that histone deacetylase and DNA methyltransferase

inhibitors interfere with MDSC chemotaxis (36, 47). Collectively, these findings suggest a mechanism through which cell adhesion and migration programs are epigenetically regulated in MDSCs and bring up the possibility of targeting distinct functions of MDSC subsets with epigenetic modifiers.

To further study the consequence of an enriched cell adhesion signature, we investigated the role of integrins that were previously linked to leukocyte migration. mMDSC-mediated acceleration of tumorigenesis was in part informed by surface integrin β1 expression, as blockade of this molecule abrogated the function of adoptively transferred mMDSCs. Integrin β1 was higher in not only mouse mMDSCs but also human mMDSCs compared with gMDSCs, indicating the conservation of this potential therapeutic target across species. Integrin β1 can form complexes with multiple α subunits, which determines ligand recognition and cellular interaction. Although the individual role of specific α subunits in mMDSCs warrants further exploration, earlier studies showed that α4β1 is important for tumor trafficking of myeloid cells, and that inhibition of the PI3Kγ–α4 signaling axis reduced the frequency of bulk MDSCs in lung and pancreatic cancer models (48, 49). Nonetheless, the levels

of phosphorylated Akt, which is downstream of PI3K, were similar between MDSC subsets, suggesting that this signaling axis may not contribute to the differential behavior of mMDSCs versus gMDSCs in GBM. Therefore, we mapped ATAC-seq gene targets to a patient single-cell dataset to identify additional regulators of mMDSC cell adhesion behavior. Importantly, CCR2, an axis previously implicated in mMDSC trafficking, was among the genes differentially expressed by mMDSCs (14). DPP-4 also emerged as a top candidate as previous studies reported an interaction between DPP-4 and integrin β1 in endothelial cells (44). Correspondingly, pharmaceutical inhibition of DPP-4 reduced migration of mMDSCs towards tumor cells *in vitro*, providing further support for the role of this molecule in myeloid cell chemotaxis. DPP-4 is a serine exopeptidase that can cleave a number of substrates, including multiple chemokines (50). Although it remains unknown whether DPP-4 interferes with mMDSC migration by modulating chemokine availability, our results indicate that it down-regulates ERK signaling, which was also previously reported in THP-1 acute monocytic leukemia cells (51). As the integrin β1–ERK signaling axis was previously linked to glioma cell invasiveness and chemoresistance (52), reducing ERK by targeting DPP-4 could have broader implications for cancer cells.

In summary, our findings highlight a role for integrin β1 and DPP-4 as immunotherapy targets in GBM. We observed that adoptive transfer of mMDSCs led to an increase in tumor-associated macrophages, which was abrogated by blockade of surface integrin β1 on mMDSCs, whereas DPP-4 inhibition reduced macrophage abundance. These findings underscore the importance of macrophages in GBM microenvironment and further support studying mMDSC-macrophage lineage relationship and communication mechanisms. Importantly, DPP-4 inhibitor treatment also led to a reduction in other immune populations, albeit at a lower extent. This could be an indirect consequence of tumor shrinkage as well as expression of DPP-4 on other cell types, including T cells (50). Although DPP-4 inhibition did not induce direct tumor cell death or lead to changes in activation/exhaustion marker expression by tumor-infiltrating CD8^{+} T-cell population, sitagliptin induced proliferation of splenic T cells *in vitro* (Supplementary Figs. S6L and S6M). Therefore, broader effect of DPP-4 inhibitors on leukocytes as well as the precise mechanism by which integrin β1 and DPP-4 regulate mMDSC-macrophage communication remain to be investigated. Our current results establish that the cell adhesion machinery is inherently different between MDSC subsets, with mMDSCs having higher integrin β1 and DPP-4 expression, which has functional consequences on the tumor-immune microenvironment. Integrin β1 expression correlates with poor GBM outcome and is upregulated in GBM models resistant to anti-angiogenic therapy (53, 54). Given that integrin β1 also plays a role in GBM cell proliferation and self-renewal (53, 54), future development of integrin β1 targeting strategies might have the dual benefit of targeting tumor cells. However, ubiquitous expression of integrin β1 as well as its role in normal brain function are potential limitations of such approaches. To this end, DPP-4 may be a good candidate. Several small molecule inhibitors of DPP-4 are widely used to treat type II diabetes (50). Repurposing these drugs as anticancer treatment strategies can modulate the immune response and is broadly applicable to other cancers that are characterized by enhanced mMDSC infiltration.

Authors' Contributions

D. Bayik: Conceptualization, data curation, formal analysis, supervision, funding acquisition, validation, investigation, visualization, writing–original draft. **C.F. Bartels:** Data curation, formal analysis, investigation, writing–review and editing. **K. Lovrenert:** Formal analysis, investigation, visualization, writing–review and editing. **D.C. Watson:** Data curation, investigation, writing–review and editing. **D. Zhang:** Formal analysis, visualization, writing–review and editing. **K. Kay:** Investigation, writing–review and editing. **J. Lee:** Investigation, writing–review and editing. **A. Lauko:** Investigation, writing–review and editing. **S. Johnson:** Investigation, writing–review and editing. **A. Lo:** Investigation, writing–review and editing. **D.J. Silver:** Investigation, writing–review and editing. **M. McGraw:** Resources, writing–review and editing. **M.Grabowski:** Resources, writing–review and editing. **A.M. Mohammadi:** Resources, writing–review and editing. **F. Veglia:** Validation, writing–review and editing. **Y. Fan:** Supervision, writing–review and editing. **M.A. Vogelbaum:** Supervision, writing–review and editing. **P. Scacheri:** Supervision, writing–review and editing. **J.D. Lathia:** Conceptualization, supervision, funding acquisition, writing–original draft.

Note

Supplementary data for this article are available at Cancer Research Online (http://cancerres.aacrjournals.org/).

References

1. De Leo A, Ugolini A, Veglia F. Myeloid cells in glioblastoma microenvironment. Cells 2020;10:18.
2. Kamran N, Kadiyala P, Saxena M, Candolfi M, Li Y, Moreno-Ayala MA, et al. Immunosuppressive myeloid cells' blockade in the glioma microenvironment enhances the efficacy of immune-stimulatory gene therapy. Mol Ther 2017;25: 232–48.
3. Antonios JP, Soto H, Everson RG, Moughon D, Orpilla JR, Shin NP, et al. Immunosuppressive tumor-infiltrating myeloid cells mediate adaptive immune resistance via a PD-1/PD-L1 mechanism in glioblastoma. Neuro Oncol 2017;19:796–807.
4. Zhang P, Miska J, Lee-Chang C, Rashidi A, Panek WK, An S, et al. Therapeutic targeting of tumor-associated myeloid cells synergizes with radiation therapy for glioblastoma. Proc Natl Acad Sci U S A 2019;116:23714–23.
5. Alban TJ, Alvarado AG, Sorensen MD, Bayik D, Volovetz J, Serbinowski E, et al. Global immune fingerprinting in glioblastoma patient peripheral blood reveals immune-suppression signatures associated with prognosis. JCI Insight 2018;3:e122264.
6. Raychaudhuri B, Rayman P, Huang P, Grabowski M, Hambardzumyan D, Finke JH, et al. Myeloid derived suppressor cell infiltration of murine and human

gliomas is associated with reduction of tumor infiltrating lymphocytes. J Neurooncol 2015;122:293–301.

7. Raychaudhuri B, Rayman P, Ireland J, Ko J, Rini B, Borden EC, et al. Myeloid-derived suppressor cell accumulation and function in patients with newly diagnosed glioblastoma. Neuro Oncol 2011;13:591–9.

8. De Cicco P, Ercolano G, Ianaro A. The new Era of cancer immunotherapy: targeting myeloid-derived suppressor cells to overcome immune evasion. Front Immunol 2020;11:1680.

9. Law AMK, Valdes-Mora F, Gallego-Ortega D. Myeloid-derived suppressor cells as a therapeutic target for cancer. Cells 2020;9:561.

10. Peereboom DM, Alban TJ, Grabowski MM, Alvarado AG, Otvos B, Bayik D, et al. Metronomic capecitabine as an immune modulator in glioblastoma patients reduces myeloid-derived suppressor cells. JCI Insight 2019;4: e130748.

11. Ouzounova M, Lee E, Piranlioglu R, El Andaloussi A, Kolhe R, Demirci MF, et al. Monocytic and granulocytic myeloid derived suppressor cells differentially regulate spatiotemporal tumour plasticity during metastatic cascade. Nat Commun 2017;8: 14979.

12. Bayik D, Zhou Y, Park C, Hong C, Vail D, Silver DJ, et al. Myeloid-derived suppressor cell subsets drive glioblastoma growth in a sex-specific manner. Cancer Discov 2020;10:1210–25.

13. Alban TJ, Bayik D, Otvos B, Rabljenovic A, Leng L, Jia-Shiun L, et al. Glioblastoma myeloid-derived suppressor cell subsets express differential macrophage migration inhibitory factor receptor profiles that can be targeted to reduce immune suppression. Front Immunol 2020;11:1191.

14. Chang AL, Miska J, Wainwright DA, Dey M, Rivetta CV, Yu D, et al. CCL2 Produced by the glioma microenvironment is essential for the recruitment of regulatory T cells and myeloid-derived suppressor cells. Cancer Res 2016;76: 5671–82.

15. Buenrostro JD, Giresi PG, Zaba LC, Chang HY, Greenleaf WJ. Transposition of native chromatin for fast and sensitive epigenomic profiling of open chromatin, DNA-binding proteins and nucleosome position. Nat Methods 2013;10:1213–8.

16. Martin M. Cutadapt removes adapter sequences from high-throughput sequencing reads. EMBnetjournal 2011;17:10–2.

17. Li H. Aligning sequence reads, clone sequences and assembly contigs with BWA-MEM. arXiv 2013:arXiv:1303.3997v2 [q-bio.GN].

18. Li H, Handsaker B, Wysoker A, Fennell T, Ruan J, Homer N, et al. The sequence alignment/map format and SAMtools. Bioinformatics 2009;25:2078–9.

19. Zhang Y, Liu T, Meyer CA, Eeckhoute J, Johnson DS, Bernstein BE, et al. Model-based analysis of ChIP-Seq (MACS). Genome Biol 2008;9:R137.

20. Ramirez F, Ryan DP, Gruning B, Bhardwaj V, Kilpert F, Richter AS, et al. deepTools2: a next generation web server for deep-sequencing data analysis. Nucleic Acids Res 2016;44:W160–5.

21. Carroll TS, Liang Z, Salama R, Stark R, de Santiago I. Impact of artifact removal on ChIP quality metrics in ChIP-seq and ChIP-exo data. Front Genet 2014;5:75.

22. Thorvaldsdottir H, Robinson JT, Mesirov JP. Integrative Genomics Viewer (IGV): high-performance genomics data visualization and exploration. Brief Bioinform 2013;14:178–92.

23. Quinlan AR, Hall IM. BEDTools: a flexible suite of utilities for comparing genomic features. Bioinformatics 2010;26:841–2.

24. Love MI, Huber W, Anders S. Moderated estimation of fold change and dispersion for RNA-seq data with DESeq2. Genome Biol 2014;15:550.

25. McLean CY, Bristor D, Hiller M, Clarke SL, Schaar BT, Lowe CB, et al. GREAT improves functional interpretation of cis-regulatory regions. Nat Biotechnol 2010;28:495–501.

26. Heinz S, Benner C, Spann N, Bertolino E, Lin YC, Laslo P, et al. Simple combinations of lineage-determining transcription factors prime cis-regulatory elements required for macrophage and B cell identities. Mol Cell 2010;38:576–89.

27. Caruso FP, Garofano L, D'Angelo F, Yu K, Tang F, Yuan J, et al. A map of tumor-host interactions in glioma at single-cell resolution. Gigascience 2020; 9:giaa109.

28. Darmanis S, Sloan SA, Croote D, Mignardi M, Chernikova S, Samghababi P, et al. Single-cell RNA-seq analysis of infiltrating neoplastic cells at the migrating front of human glioblastoma. Cell Rep 2017;21:1399–1410.

29. Yuan J, Levitin HM, Frattini V, Bush EC, Boyett DM, Samanamud J, et al. Single-cell transcriptome analysis of lineage diversity in high-grade glioma. Genome Med 2018;10:57. doi: 10.1186/s13073-018-0567-9.

30. Neftel C, Laffy J, Filbin MG, Hara T, Shore ME, Rahme GJ, et al. An integrative model of cellular states, plasticity, and genetics for glioblastoma. Cell 2019;178: 835–49.e21.

31. Yu K, Hu Y, Wu F, Guo Q, Qian Z, Hu W, et al. Surveying brain tumor heterogeneity by single-cell RNA-sequencing of multi-sector biopsies. Natl Sci Rev 2020;7:1306–18.

32. Hao Y, Hao S, Andersen-Nissen E, Mauck WM 3rd, Zheng S, Butler A, et al. Integrated analysis of multimodal single-cell data. Cell 2021;184:3573–87.

33. Hafemeister C, Satija R. Normalization and variance stabilization of single-cell RNA-seq data using regularized negative binomial regression. Genome Biol 2019;20:296.

34. Alshetaiwi H, Pervolarakis N, McIntyre LL, Ma D, Nguyen Q, Rath JA, et al. Defining the emergence of myeloid-derived suppressor cells in breast cancer using single-cell transcriptomics. Sci Immunol 2020;5:eaay6017.

35. Mastio J, Condamine T, Dominguez G, Kossenkov AV, Donthireddy L, Veglia F, et al. Identification of monocyte-like precursors of granulocytes in cancer as a mechanism for accumulation of PMN-MDSCs. J Exp Med 2019;216: 2150–69.

36. Nair VS, Saleh R, Toor SM, Taha RZ, Ahmed AA, Kurer MA, et al. Transcriptomic profiling disclosed the role of DNA methylation and histone modifications in tumor-infiltrating myeloid-derived suppressor cell subsets in colorectal cancer. Clin Epigenetics 2020;12:13.

37. Kurotaki D, Yamamoto M, Nishiyama A, Uno K, Ban T, Ichino M, et al. IRF8 inhibits C/EBPalpha activity to restrain mononuclear phagocyte progenitors from differentiating into neutrophils. Nat Commun 2014;5:4978.

38. Netherby CS, Messmer MN, Burkard-Mandel L, Colligan S, Miller A, Gomez EC, et al. The granulocyte progenitor stage is a key target of IRF8-mediated regulation of Myeloid-derived suppressor cell production. J Immunol 2017; 198:4129–39.

39. Harjunpaa H, Asens ML, Guenther C, Fagerholm SC. Cell adhesion molecules and their roles and regulation in the immune and tumor microenvironment. Front Immunol 2019;10:1078.

40. Desgrosellier JS, Cheresh DA. Integrins in cancer: biological implications and therapeutic opportunities. Nat Rev Cancer 2010;10:9–22.

41. Corzo CA, Condamine T, Lu L, Cotter MJ, Youn JI, Cheng P, et al. HIF-1alpha regulates function and differentiation of myeloid-derived suppressor cells in the tumor microenvironment. J Exp Med 2010;207:2439–53.

42. Kwak T, Wang F, Deng H, Condamine T, Kumar V, Perego M, et al. Distinct populations of immune-suppressive macrophages differentiate from monocytic Myeloid-derived suppressor cells in cancer. Cell Rep 2020;33:108571.

43. Beury DW, Parker KH, Nyandjo M, Sinha P, Carter KA, Ostrand-Rosenberg S. Cross-talk among myeloid-derived suppressor cells, macrophages, and tumor cells impacts the inflammatory milieu of solid tumors. J Leukoc Biol 2014;96: 1109–18.

44. Shi S, Srivastava SP, Kanasaki M, He J, Kitada M, Nagai T, et al. Interactions of DPP-4 and integrin beta1 influences endothelial-to-mesenchymal transition. Kidney Int 2015;88:479–89.

45. Sampson JH, Gunn MD, Fecci PE, Ashley DM. Brain immunology and immunotherapy in brain tumours. Nat Rev Cancer 2020;20:12–25.

46. Genoud V, Marinari E, Nikolaev SI, Castle JC, Bukur V, Dietrich PY, et al. Responsiveness to anti-PD-1 and anti-CTLA-4 immune checkpoint blockade in SB28 and GL261 mouse glioma models. Oncoimmunology 2018;7:e1501137.

47. Lu Z, Zou J, Li S, Topper MJ, Tao Y, Zhang H, et al. Epigenetic therapy inhibits metastases by disrupting premetastatic niches. Nature 2020;579:284–90.

48. Jin H, Su J, Garmy-Susini B, Kleeman J, Varner J. Integrin alpha4beta1 promotes monocyte trafficking and angiogenesis in tumors. Cancer Res 2006;66:2146–52.

49. Schmid MC, Franco I, Kang SW, Hirsch E, Quilliam LA, Varner JA. PI3-kinase gamma promotes Rap1a-mediated activation of myeloid cell integrin alpha4-beta1, leading to tumor inflammation and growth. PLoS One 2013;8:e60226.

50. Mulvihill EE, Drucker DJ. Pharmacology, physiology, and mechanisms of action of dipeptidyl peptidase-4 inhibitors. Endocr Rev 2014;35:992–1019.

51. Ervinna N, Mita T, Yasunari E, Azuma K, Tanaka R, Fujimura S, et al. Anagliptin, a DPP-4 inhibitor, suppresses proliferation of vascular smooth muscles and monocyte inflammatory reaction and attenuates atherosclerosis in male apo E-deficient mice. Endocrinology 2013;154:1260–70.

52. Han S, Li Z, Master LM, Master ZW, Wu A. Exogenous IGFBP-2 promotes proliferation, invasion, and chemoresistance to temozolomide in glioma cells via the integrin beta1-ERK pathway. Br J Cancer 2014;111:1400–9.

53. Carbonell WS, DeLay M, Jahangiri A, Park CC, Aghi MK. beta1 integrin targeting potentiates antiangiogenic therapy and inhibits the growth of bevacizumab-resistant glioblastoma. Cancer Res 2013;73:3145–54.

54. Malric L, Monferran S, Gilhodes J, Boyrie S, Dahan P, Skuli N, et al. Interest of integrins targeting in glioblastoma according to tumor heterogeneity and cancer stem cell paradigm: an update. Oncotarget 2017;8:86947–68.